RSC Advances

PAPER

View Article Online
View Journal | View Issue

Cite this: *RSC Adv.*, 2020, **10**, 1901

Repair of segmental rabbit radial defects with Cu/Zn co-doped calcium phosphate scaffolds incorporating GDF-5 carrier†

Chengdong Zhang, ‡[a] Fei Yang,‡[a] Dongqin Xiao, [ab] Qiao Zhao,[a] Shuo Chen,[a] Kang Liu,[a] Bo Zhang,[a] Gang Feng*[a] and Ke Duan*[c]

Repair of segmental bone defects is a challenge in orthopaedics. A bone substitute is a potential solution for this challenge, and angiogenesis and osteogenesis are critical to the performance of scaffold materials. For enhancing angiogenesis and osteogenesis activities of implanted scaffolds, Cu/Zn co-doped calcium phosphate scaffolds carrying GDF-5-release microspheres were prepared and implanted into surgically created critical-sized rabbit radial defects. Radiological examination, histological analysis and biomechanical tests were used to evaluate the bone healing-union. Results showed that, with increasing Cu/Zn concentrations, new bone area, new blood vessel density, and bending failure load all increased significantly. Furthermore, Cu/Zn co-doped scaffolds incorporating GDF-5-release microspheres exhibited further increased angiogenesis and osteogenesis (*vs.* Cu/Zn co-doped alone), as well as a superior bending failure load. These show that, simultaneous incorporation of trace essential ions and GDF-5 combines pro-angiogenic and pro-osteogenic actions of these bioactive substances, potentially offering an effective approach to assist the healing of critical-sized bone defects.

Received 18th November 2019
Accepted 19th December 2019

DOI: 10.1039/c9ra09626d

rsc.li/rsc-advances

Introduction

The repair of large bone defects remains difficult in orthopaedics. Autografting has been the gold standard for this task, but its use is restricted by limited autograft availability and the requirement of an additional operation. Synthetic bone-substituting materials, primarily calcium phosphates (CaPs) in various porous forms, have been intensively studied for this application, but their osteogenesis and resorption rates are generally less satisfactory than autografts.[1,2] This is partly explained by the nature of human bones, which comprise nano-sized non-stoichiometric apatite crystals that are more resorbable (*vs.* synthetic stoichiometric CaPs of conventional grain sizes) and a collagenous matrix harboring a variety of signal molecules (*e.g.*, growth factors).[3,4] In fact, demineralized bone matrix (DBM) itself is used clinically to assist the repair of bone defects, where it releases signal molecules to accelerate osteogenesis.[5] Bone repair involves a cascade of critical events, such as the migration of osteoblast progenitor cells to the defect, their differentiation to osteoblasts, and production of a calcified matrix.[6,7] Moreover, angiogenesis is also a key factor in osteogenesis, as it supplies nutrients to sustain new bone formation.[8] CaPs alone, with their relatively simple chemistry, may not effectively regulate these events to expedite bone repair. Conversely, it follows that, introduction of biofunctional substances to CaPs may be an effective approach to improving their clinical performance.

Bone morphogenetic proteins (BMPs) are the first family of mammalian morphogens identified.[9] First isolated from DBM, BMPs potently induce bone formation in skeletal and non-skeletal tissues. A large number of studies have reported local release of BMPs, frequently BMP-2, to accelerate bone defect healing.[10,11] However, other experimental studies and recent reports on commercial products indicated side-effects of BMP-2 such as ossification in adjacent non-targeted sites, indicating the need to explore safer alternatives.[12–14] Growth differentiation factor-5 (GDF-5) is another member of the BMP family and was reported to be essential for normal bone and joint formation.[15,16] Earlier studies found GDF-5 to induce chondrogenic differentiation of mesenchymal stem cells (MSCs).[17,18] More recent works reported the stimulation of osteoblastic differentiation of MSCs *in vitro* and osteogenesis *in vivo* by this GDF-5.[19,20] Additionally, GDF-5 was observed to promote the recruitment of MSCs and their production of vascular endothelial growth factor (VEGF).[21] Leknes *et al.* reported that,

[a]*Research Institute of Tissue Engineering and Stem Cells, Nanchong Central Hospital, The Second Clinical College of North Sichuan Medical College, Nanchong, Sichuan, 637000 China. E-mail: fenggangncch@163.com; keduan@swmu.edu.cn*

[b]*MERLN Institute for Technology-Inspired Regenerative Medicine, Department of Complex Tissue Regeneration, Maastricht University, Maastricht, Netherlands*

[c]*Sichuan Provincial Laboratory of Orthopaedic Engineering, Department of Bone and Joint Surgery, Affiliated Hospital of Southwest Medical University, Luzhou, Sichuan, 646000 China*

† Electronic supplementary information (ESI) available. See DOI: 10.1039/c9ra09626d

‡ Authors contributed equally to this work.

compared with BMP-2, local use of GDF-5 elicited less adverse effects such as ectopic bone formation, extensive bone resorption (remodeling), and seroma formation.[22] These findings suggest this protein to be a potential substitute for BMP-2.

In addition to growth factors, essential inorganic ions represent another class of signals affecting osteogenesis, as they participate in numerous critical signaling pathways.[23,24] For example, zinc (Zn) is a trace element essential for normal skeletal development.[25] At cellular levels, Zn promotes osteoblastic differentiation of MSCs *in vitro* and increases osteogenesis *in vivo* by enhancing collagen synthesis, alkaline phosphatase (ALP) activity, and collagen matrix calcification by osteoblasts.[26,27] Copper (Cu) is a cofactor for several important enzymes, and it is essential for crosslinking of collagen fibers in bones.[28] Studies have indicated that, Cu promotes angiogenesis by stimulating endothelial cell proliferation and upregulating VEGF expression.[29] CaP scaffolds doped with Zn or Cu have been observed to improve *in vivo* vascularization, osteoinduction in muscles, and osteogenesis in skeletal defects.[30]

In an attempt to simultaneously modulate multiple events in bone repair (*i.e.*, angiogenesis and osteogenesis), we prepared porous CaP scaffolds containing various concentrations of Cu and Zn dopants and GDF-5-loaded polymer microspheres, and implanted them in rabbits segmental bone defects. Osteogenesis, angiogenesis, and recovery of mechanical strength were evaluated by radiography, histology and mechanical tests.

Experimental

Scaffolds preparation

Cu/Zn-doped CaP slurries were synthesized by precipitation reactions between calcium nitrate [$(CaNO_3)_2 \cdot 4H_2O$] and ammonium monohydrogen phosphate [$(NH_4)_2HPO_4$] under various concentrations of Cu^{2+} and Zn^{2+} (Table 1).[31] BCP scaffolds were prepared by infiltration of a slurry through a packed bed of alginate hydrogel beads (Fig. 1) followed by drying and sintering (1200 °C, 2 h).[32] The scaffolds were named according to increasing Cu/Zn concentrations as P0, P1, and P2 (Table 1). Additionally, GDF-5-loaded PLGA microspheres were synthesized by an emulsion method[31] and attached to P2 scaffolds by vacuum drying (0.5 mg of microspheres/scaffold). These scaffolds were named P2/GDF-5.

Characterization of scaffolds

Crystal phase structures were measured by X-ray diffraction (XRD, Panalytical X'PertPro MPD, Cu Kα, 35 mA, 45 kV). The morphology and elemental composition of the scaffolds were characterized with a scanning electron microscopy (SEM, JEOL JSM7001F) equipped with an energy dispersive X-ray (EDX) spectrometer. The ion release kinetics from the scaffolds were determined by immersing each scaffold in a 50 mM Tris–NaCl buffer (3 mL, pH = 7.4) and analyzing the supernatant by inductively coupled plasma mass spectrometry (ICP-MS, Elan DRC-e, PerkinElmer). The total amount of ions was extracted by completely dissolving the scaffolds into diluted nitric acid (0.37 mol L^{-1}) and the supernatant was measured by ICP-MS. The GDF-5 release kinetics from the scaffolds P2/GDF-5 were determined by immersing each sample in 2 mL of phosphate-buffered saline (PBS, 0.01 M, pH = 7.4) and analysing the supernatant with enzyme-linked immunosorbent assay (ELISA) kits (Cusabio Biotech, Wuhan, Hubei, China) following the manufacturer's instructions.

Table 1 Conditions of scaffold preparation and characteristics of scaffolds obtained (n = 3)

	Preparation conditions			Scaffold characteristics (molar ratio)	
Scaffold	Ca (M)	Cu (M)	Zn (M)	Phase ratio (β-TCP/HA)	Element ratio (Cu/Zn/Ca)
P0	0.85	—	—	59/41	—
P1	0.84	0.005	0.005	64/36	0.005/0.004/1
P2	0.81	0.02	0.02	70/30	0.01/0.009/1

Animals and operation

All animal procedures were performed in accordance with the Guide for the Care and Use of Laboratory Animals of the National Institutes of Health and approved by the Animal Ethics Committee of North Sichuan Medical College. Fifty New Zealand White rabbits (3 months, 2.5–3.0 kg, 25 male, 25 female; Center of Laboratory Animals, North Sichuan Medical College, Nanchong, Sichuan, China) were randomly divided into a blank control group and four experimental groups (10 animals per group; 5 male, 5 female). The animal was anesthetized by intravenous injection of 2% pentobarbital sodium (1.5 mL kg^{-1}). A longitudinal incision (3 cm) was made over the middle third of the radius and separated to expose the periosteum. A 15 mm segment was marked on the radius, and the periosteum in the segment was completely removed with a scalpel. The radius in the segmented was resected with a dental abrasive drill (Fig. 2). For the blank control group, the defect was left unfilled and the wound sutured layer by layer. For the experimental groups, a scaffold was implanted in the defect without subsequent placement of internal fixation, and the wound closed identically. Correspondingly, the four experimental groups were named according to the scaffolds implanted as P0, P1, P2, and P2/GDF-5.

After operation, the animal received intravenous penicillin (6000 IU kg^{-1}) for 3 d. All animals were caged separately in the Center of Laboratory Animals of North Sichuan Medical College, allowed free access to water and diet, and monitored regularly for adverse events (*e.g.*, bone fracture, infection, death).

Radiography

At 4, 8, and 12 weeks after operation, radiographs were taken evaluated using the Lane–Sandhu scoring system (Table 2).[33]

Histology and histomorphometry

At 12 weeks after operation, animals were killed by pentobarbital overdosing. The radii of three animals per group were collected and cut to ~3 mm thickness. They were fixed in paraformaldehyde (4%, 24 h), decalcified in 10%

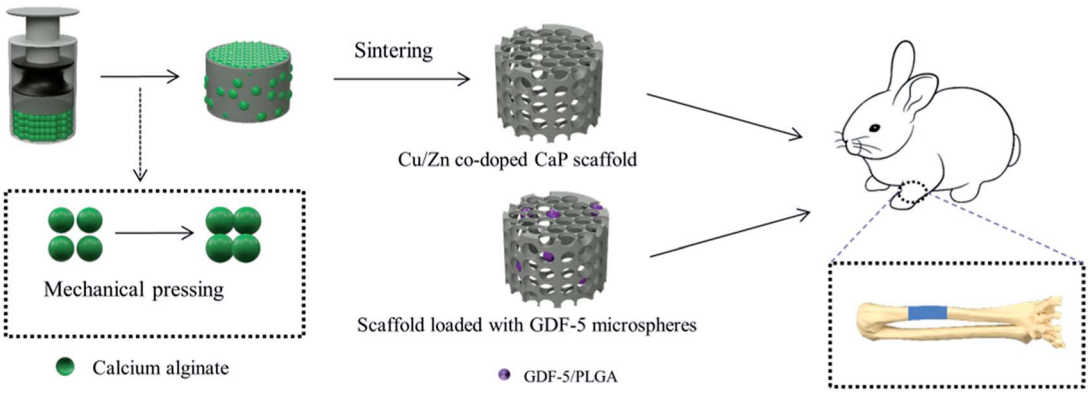

Fig. 1 Schematic illustration of scaffold preparation and repair of segmental bone defect in rabbit radius. Cu/Zn co-doped porous scaffolds were prepared by infiltration of a slurry through a packed bed of alginate hydrogel beads followed by sintering. Then, porous scaffolds and scaffolds loaded with GDF-5 carrier were implanted into the rabbit radius defect.

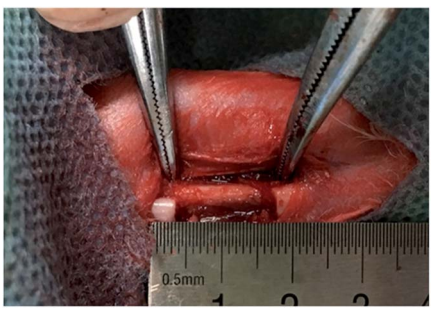

Fig. 2 Intraoperative photograph showing preparation of a segmental defect in a rabbit radius.

ethylenediamine tetraacetic acid (37 °C, 72 h) with frequent examinations of hardness, and finally rinsed with copious water (2 h × 3). The decalcified samples were dehydrated in ethanol series (70–100%), mounted in paraffin, sectioned (~4 μm) in the middle third of the defect and perpendicular to the longitudinal axis of the radius. Subsequently, the sections (three sections per rabbit) were stained separately with Hematoxylin-Eosin (HE) and Masson's trichrome reagent following standard procedures.[34,35] Stained sections were observed under an inverted phase-contrast light microscope (Leica DMi8). Micrographs were captured and analyzed (ImagePro, MediaCybernetics, Bethesda, MD, USA) for new blood vessels and new bone areas. Five sequential sections per group were selected for evaluation.

Biomechanical test

Twelve weeks after operation, three radius-ulna constructs of each group ($n = 5$) were tested by three-point bending (Instron 5567, Instron, USA) until rupture.[36] Briefly, the defective radius and adjoining ulna were placed on two supports (distance: 20 mm), and a bending load was applied at the midpoint of the defect at 1 mm min^{-1} until rupture.

Statistical analysis

Data were compared by analysis of variance (ANOVA; SPSS 15, SPSS, Chicago, IL, USA) and subsequent Tukey tests for multiple comparisons. A p-value <0.05 was considered statistically significant.

Results and discussions

Scaffold characteristics

All scaffolds had interconnected porous structures with pore sizes of 200–600 μm (Fig. 3A). Higher magnification observations revealed that, the surface of the scaffold P0 consisted of

Table 2 Lane–Sandhu criteria and scores for evaluation of bone fracture/defect healing

Event	Radiographic findings	Score
Bone formation	No new bone/callus	0
	New bone/callus ≥ 25% of defect area	1
	New bone/callus ≥ 50% of defect area	2
	New bone/callus ≥ 75% of defect area	3
	New bone/callus = 100% of defect area	4
Bone union	Fracture line evident	0
	Fracture line partly visible	2
	Fracture line invisible	4
Bone remodeling	No sign of medullary cavity remodeling	0
	Formation of medullary cavity	2
	Canalization of medullary cavity and cortex formation	4

crystalline grains (size: ~1 μm) (Fig. 3B), whereas the surface of P1 featured discrete cubic nanoparticles (size: ~200 nm) (Fig. 3C) and that of P2 presented rough microparticles (size: 0.5–10 μm) (Fig. 3D). EDX mapping of the scaffold P2 (Fig. 3F) revealed a small amount of Cu and Zn uniformly scattered throughout the surface. Chemical analyses by ICP-MS found Cu/Zn/Ca molar ratios to be 0.005/0.004/1 for P0 and 0.001/0.009/1 for P1, both lower than the counterpart ratios of their synthetic solutions (P1: 0.005/0.005/0.84, P2: 0.02/0.02/0.81; Table 1). XRD spectra (ESI Fig. S1†) found all scaffolds to be composed of β-tricalcium phosphate (β-TCP) and hydroxyapatite (HA) in different fractions (Table 1). The β-TCP/HA ratio increased with the Cu and Zn concentrations in the synthetic solution. In *in vitro* release of the scaffold P2 (Fig. 4A), both Cu and Zn exhibited a sustained and controlled release profile for up to one month. Zn cumulative release showed a substantially higher release rate than Cu, while Ca showed the fastest cumulative release. The cumulative release of Cu and Zn reached ~19% after 30 d, accompany by ~2% Ca cumulative release. Moreover, the surface of P2/GDF-5 was decorated by PLGA microspheres containing GDF-5 (diameter: 3–20 μm) (Fig. 3E). ELISA indicated that, the microspheres contained 5.21 ± 1.32% (w/w) of GDF-5, and produced a burst release in the first 2 d followed by a sustained release up to 30 d (cumulative release: ~900 ng mL^{-1}) (Fig. 4B), exhibiting a well sustained GDF-5 release for GDF-5-loaded scaffolds.

General observations

All animals survived until sample collection. All animals recovered normal food intake and activities after emergence from anesthesia. One rabbit developed postoperative wound infection, and it was resolved by cleaning and local antiseptic treatment.

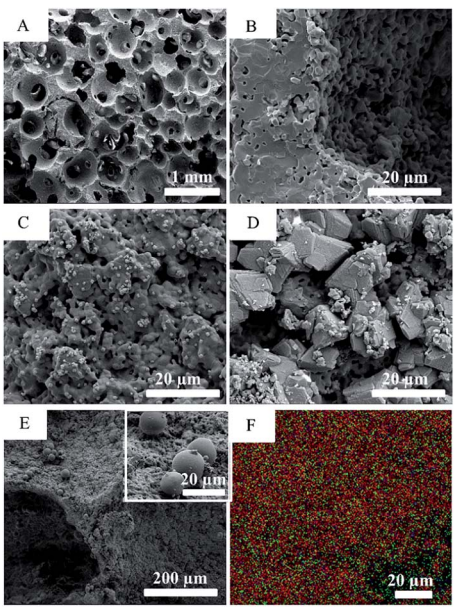

Fig. 3 SEM images of (A) porous scaffolds and surface structures of (B) P0, (C) P1, (D) P2, and (E) P2/GDF-5; (F) EDX mapping showing element distribution on surface of P2 (red: calcium, green: copper, purple: zinc).

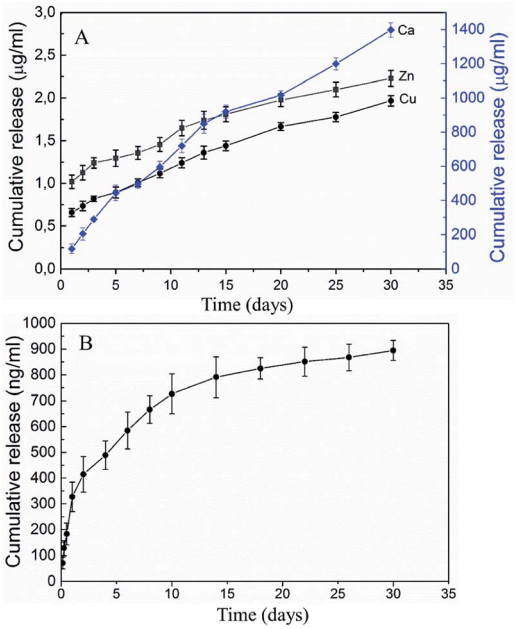

Fig. 4 The cumulative release profiles of metallic ions from scaffold P2 (A) and GDF-5 from the scaffold P2/GDF-5 (B) (mean ± standard deviation, $n = 3$).

Radiographic evaluation

At week 4, the radiographs of all groups (Fig. 5) showed evident osteotomy defects and limited new bone formation at the osteotomy ends adjacent to the periosteum. All scaffolds were retained in the defect without evident dislocation. The scaffold in the P2/GDF-5 group appeared to be bridged to the osteotomy ends by low-density callus. In comparison, scaffolds in the other groups were separated from the osteotomy ends by clear lines.

At week 8 (Fig. 5), the defect of the blank control group showed cancellous bone formation. All experimental groups showed partial degradation of scaffolds, with higher degrees of degradation seen in groups P2 and P2/GDF-5 than in P0 and P1. Additionally, P0 had slight signs of cortical bone formation but without bony union between the osteotomy ends and the scaffold. In comparison, P1, P2, and P2/GDF-5 developed bony union of scaffold and osteotomy ends on the ulnar aspect. The areas of bony union were estimated to follow the rank: blank control < P0 < P1 < P2 < P2/GDF-5.

At week 12, the defect in the blank control group remained largely open but with local cortical bone formation, generally similar to the status at week 8. Scaffolds in P1, P2, and P2/GDF-5 were largely replaced by new bone, whereas that in P0 remained relatively intact. P0 developed cortical bone at osteotomy ends, with moderate bony union with the scaffold on the ulnar aspect. P1 had increased bony union and further cortical bone formation in the defect compared with week 8. P2 and P2/GDF-5 showed nearly complete defect healing, with continuous cortex and canalization. Practically no residual scaffold material could be seen in the radiographs of P2 and P2/GDF-5. The extents of defect healing were estimated to follow the rank: blank control < P0 < P1 < P2 < P2/GDF-5.

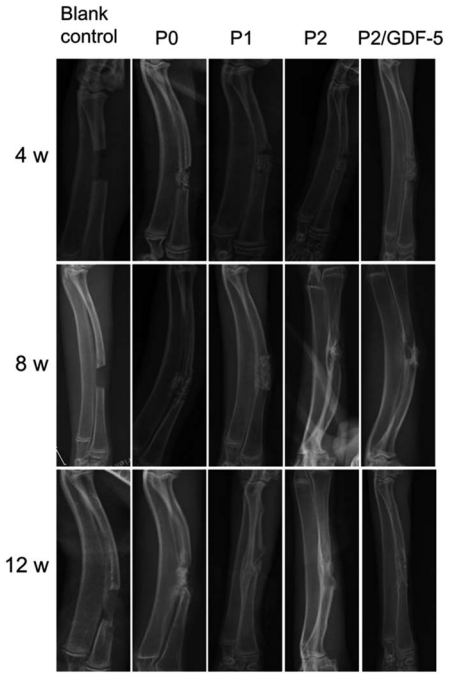

Fig. 5 Radiographs taken 4, 8, and 12 weeks after operation.

At week 4, the Lane–Sandhu score recorded from P2/GDF-5 was significantly higher than those of all other groups (all $p < 0.05$) (Table 3), and the scores from P2 and P1 were significantly higher than those from P0 and blank control (all $p < 0.05$). At week 8, the score of P2/GDF-5 was again significantly higher than those of all other groups (all $p < 0.05$); the difference between following group pairs were also statistically significant: P2–blank control ($p = 0.0003$), P2–P0 ($p = 0.0005$), P1–blank control ($p = 0.0005$) and P1–P0 ($p = 0.002$). At week 12, there were significant differences among all groups (all $p < 0.05$); the scores followed the rank: P2/GDF-5 > group P2 > group P1 > group P0 > group blank control.

Histology and histomorphometry

HE staining revealed that samples collected at week 12 (Fig. 6) showed no signs of inflammatory response, toxicity, or immune rejection in any group. The blank control group formed granulation tissues in the defect, without recognizable new bone. P0 formed osteoid tissues growing along the scaffold surface. In comparison, abundant new bone formation was seen in P1, P2, and P2/GDF-5. In P1, the new bone tissue appeared to be somewhat parallel to the interstices available for ingrowth. In P2 and P2/GDF-5, the new bone was woven in morphology. In comparison, P2/GDF-5 showed improved remodeling-canalization of the medullary cavity (*vs.* P2) and had more new blood vessels than did other groups (blank control, P0, P1 and P2).

Masson trichrome staining (Fig. 7) revealed generally consistent findings to HE-stained sections. The blank control group formed abundant granulation tissues and new vessels, but without noticeable new bone formation. P0 formed new bone, frequently along the scaffold surface. P1, P2, and P2/GDF-5 had extensive new bone formation and blood vessel ingrowth; the new bone tissue in P2 and P2/GDF-5 appeared woven in nature and visibly larger than that formed in P1. Moreover, P2/GDF-5 exhibited a more mature remodeling-canalization and greater blood vessel density compared with all other groups.

New bone area and blood vessel counts at week 12 were measured from sections stained with Masson trichrome reagent and HE, respectively. It was observed that, P3 and P2 had significantly higher new bone area fractions than all other groups (all $p < 0.05$; Fig. 8). Additionally, P1 had a significantly higher new bone area fraction than P0 and the blank control (both $p < 0.05$), and P0 also had a significantly higher value compared with the blank control ($p < 0.05$).

P3 had a significantly higher new blood vessel density compared with all other groups (all $p < 0.05$). Notably, the blank control and P2 had significantly higher new blood vessel densities compared with P0 and P1 ($p < 0.05$). The high new vessel density recorded in the blank control (only next to P2/GDF-5) was attributable to its active formation of granulation tissues.

Table 3 Lane–Sandhu scores recorded 4–12 weeks after operation (mean ± standard deviation, $n = 5$)

Group	4 weeks	8 weeks	12 weeks
Blank control	0.17 ± 0.41	0.57 ± 0.52	1.17 ± 0.41
P0	0.50 ± 0.55	1.83 ± 0.99	3.50 ± 0.55
P1	0.83 ± 0.41	3.83 ± 0.98	5.83 ± 0.98
P2	1.17 ± 0.41	4.17 ± 0.41	7.51 ± 0.84
P2/GDF-5	2.33 ± 1.03	6.83 ± 0.98	10.57 ± 1.03

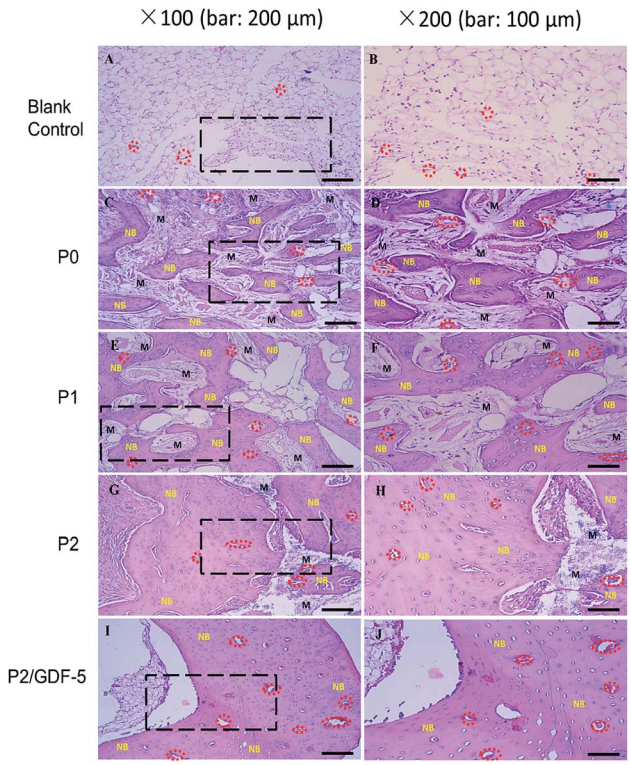

Fig. 6 Light micrographs of hemoatoxylin-eosin stained sections prepared from samples collected 12 weeks after operation (NB: new bone; M: materials; red circle: blood vessel).

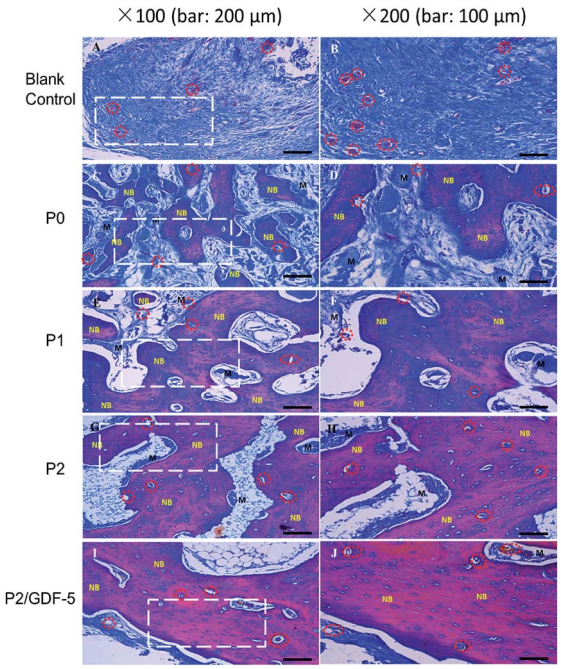

Fig. 7 Light micrographs of Masson's trichrome stained section prepared from samples collected 12 weeks after operation (NB: new bone; M: materials; red circle: blood vessel).

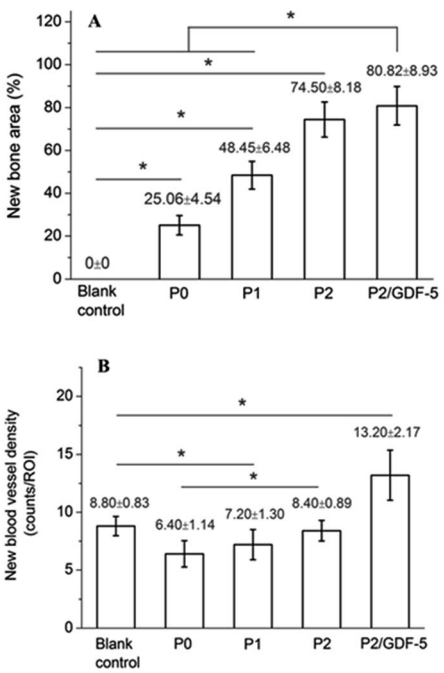

Fig. 8 (A) New bone and (B) new blood vessel formation in samples collected at week 12 (mean ± standard deviation, $n = 5$); *$p < 0.05$.

Bending failure load

At week 12, the radius-ulna complex was tested by bending to evaluate the status of mechanical recovery. The bending failure loads increased in an order of: blank control < P0 < P1 < P2 < P2/GDF-5 (Fig. 9). As P0 and P1 had undergone only limited

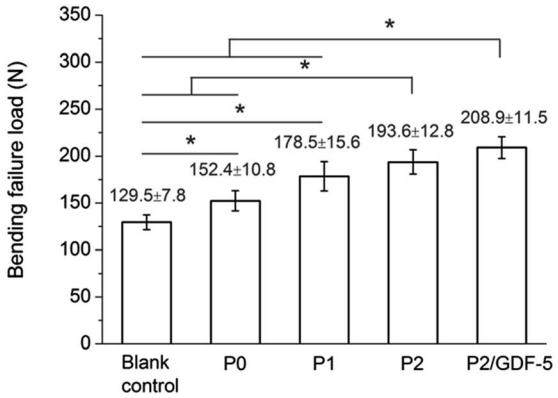

Fig. 9 Three-point bending failure loads of operated radius-ulna constructs measured at week 12 (mean ± standard deviation, $n = 5$); *$p < 0.05$.

osteogenesis at week 12, the defect remained largely non-united and the bending load was borne primarily by the adjoining ulna. P0 and P1 were both significantly higher than the blank control, and P1 was significantly higher than P0. P2 was significantly higher than the blank control and P0, but the difference between P2 and P1 was not statistically significant ($p = 0.12$). P2/GDF-5 was significantly higher than the blank control, P0, and P1, but the difference between P2/GDF-5 and P2 was not statistically significant ($p = 0.09$). Furthermore, compared with the failure load of unoperated radius-ulna constructs collected from the rabbits (245.9 ± 6.2 N), the load measured from P2/GDF-5 was only 15% lower. In contrast, all other groups remained significantly lower than the unoperated constructs (all $p < 0.05$).

Discussion

Findings of the present study show that, with the combination of signal substances (*e.g.*, Zn, Cu, GDF-5) and porous CaP scaffolds, the repair critical-sized bone defects can be substantially improved. Under the optimum conditions used (P2/GDF-5), the osteotomized radii recovered 85% of the failure load at week 12, practically allowing resumption of normal locomotion.

Critical-sized segmental skeletal defects are difficult to heal without assistance. It is generally accepted that, a segmental defect can be considered critical-sized when the length/diameter ratio is ≥1.5.[37] In the present study, a 15 mm segment of the radius and the overlying periosteum was removed, creating a length/diameter ratio of ~3.5, far exceeding 1.5 (Fig. 2). Therefore, the defect is critical-sized and, thus, frequently does not heal when left unfilled, as also corroborated by our blank control group (Fig. 4). In response to this limitation, many studies have combined porous CaP scaffolds with bioactive molecules to integrate their osteoconductive nature and biological function, a property possessed by the current gold standard in bone grafting (*i.e.*, autografts).

Co-doping of Zn and Cu increased new bone and blood vessel formed and the bending failure load in a dose-dependent

manner (Fig. 8 and 9). These may be explained by the physical and biological effects of these ions. Physically, with increasing doping of Zn and Cu, the fraction of β-TCP increased (Table 1), presumably because these ions reduced the thermal stability of HA crystal cells and thereby induced their decomposition to β-TCP during sintering.[38,39] Another study also reported the formation of β-TCP during HA preparation in the presence of Zn ions.[40] Compared with HA, β-TCP is more soluble and more rapidly degradable. Consequently, its degradation creates more space for bone ingrowth (*vs.* pure HA scaffold), increasing the new bone/defect area ratio. In our previous study,[31] after co-culture with cells for 5 d, flaky apatite crystals were observed on the surface of P2, whereas no apatite formed on P0 or P1 (ESI Fig. S2†). This indicates that with increasing dopant concentrations, the scaffold became more favorable for apatite deposition, consistent with the trend of new bone formation *in vivo* (Fig. 7 and 8). Other studies also observed that, Zn addition enhanced the *in vitro* bioactivity of HA, as by enhanced apatite formation during incubation in simulated body fluid, consistent with our findings.[40,41]

Biologically, many studies have shown that, Zn ions can enhance the osteogenic differentiation of bone marrow mesenchymal stem cells (BMSCs), and Cu ions can stimulate the angiogenesis of vascular endothelial cells (VECs) by increasing VEGF secretion.[42,43] Thus, Cu/Zn co-doping may have positively affected osteoblastic and angiogenic activities, as suggested by our previous experiments of *in vitro* cell culture. We previously found that, the addition of Zn^{2+} to cultured BMSCs significantly enhanced the formation of calcified nodules, whereas the addition of Cu^{2+} to VECs cultured on Matrigel-coated wells promoted the formation of capillary-like structures.[31] More importantly, the supernatant extracted from scaffolds (P2) immersed in PBS was observed to simultaneously enhance the formation of calcified nodules and capillary-like structures, indicating the key role of Cu/Zn co-doping in enhancing osteogenic and angiogenic capacities of BCP scaffold.[31] Many studies have reported positive effects of incorporating inorganic ions in CaPs,[44,45] but few have examined incorporation of multiple ions. The substantially improvement observed from P0 to P2 encourages quantitating the role of each ion and evaluating their combination effects.

Attachment of GDF-5-loaded microspheres to P2 scaffolds further increased their new bone formation, blood vessel density, and bending load, with the increase in vessel density being statistically significant (Fig. 7–9). GDF-5 has been proposed as a safer alternative to BMP-2. Numerous studies have evaluated its effect on cartilage repair, whereas relative few works have investigated its effect on bone defect healing *in vivo*, probably because it was first isolated from cartilage.[46] Wulsten *et al.*[47] compared the effects of rhGDF-5 with rhBMP-2 on the healing of rat femoral defects by implanting collagen sponges containing rhGDF-5 or rhBMP-2 (50 μg) into the defect. Six weeks after operation, the two groups had comparable mechanical properties, but the rhGDF-5 group formed cartilaginous tissue and showed delayed tissue mineralization compared with the rhBMP-2 group. To enhance the osteogenetic ability of GDF-5, Kerstin *et al.* placed collagen sponges carrying mutant GDF-5v453/v456 (with elevated BMP receptor-IA binding), BMP-2, or GDF-5 in rabbit radial defects. Mutant GDF-5v453/v456 was found to produce a superior osteogenicity to GDF-5 and a superior angiogenicity to BMP-2.[48] Additionally, Kim *et al.* compared healing of canine periodontal bone defects assisted with rhGDF-5 carried by β-TCP granules or collagen sponge,[49] and observed that rhGDF-5-loaded β-TCP significantly enhanced bone formation compared with collagen sponge carrier. Collectively, these findings indicate that the osteogenic property of GDF-5 treatments is generally lower than BMP-2 and is dose- and carrier-dependent. However, the aniogenicity of GDF-5 is superior to BMP-2, a promising aspect for long-bone defect healing, where high angiogenicity is required. To our best knowledge, our study is the first report of critical-sized long-bone defect repair assisted simultaneously by GDF-5 and trace metallic ions (Cu and Zn). GDF-5 is known to enhance the proliferation and osteoblastic differentiation of BMSCs.[19] Our previous study also confirmed that, GDF-5 released from P2/GDF-5 further enhanced osteoblastic gene expression and alkaline phosphate activity of BMSCs and VECs, as well as their production of VEGF secretion compared with scaffold P2.[31] Furthermore, *in vitro* cell culture found that, as opposed to P0–P2, P2/GDF-5 induced the formation of tubular, capillary-like structures. This effect suggests that, in our experimental conditions (*e.g.*, cell, dose, culture medium), GDF-5 was particularly effective at improving angiogenesis, consistent with the significantly increased blood vessel density recorded in P2/GDF-5 (*vs.* P2) (Fig. 8). Moreover, the GDF-5 addition played a positive role in the new bone formation and mechanical properties in rabbit radius repair. Conversely, the addition of Cu/Zn ions enhanced the osteogenesis and angiogenesis capacities of GDF-5 *in vitro* and *in vivo*, which may reduce the dose GDF-5 required (*vs.* GDF-5 release alone). Therefore, simultaneous incorporation of trace essential ions and GDF-5 shows promising potential application for long bone healing when high angiogenicity and osteogenicity are desired.

The present study includes several limitations that need to be overcome by further studies. First, Cu and Zn were co-doped rather than each varying independently; this prevents quantitation of the contribution of each and determination of their optimum concentrations. Second, the rabbits are young and thus able to heal satisfactorily, whereas older animals may be more relevant to clinics. Finally, the radial segmental defect is not a weight-bearing model, although it is necessary to achieve positive results from less challenging tests before proceeding to more difficult ones.

Conclusion

Cu/Zn co-doped CaP scaffolds carrying GDF-5 release microspheres were successfully used for repairing critical-sized rabbit radial defects. Cu/Zn co-doping effectively promoted angiogenesis, osteogenesis, and biomechanical recovery in a dose-dependent manner. GDF-5 release further enhanced angiogenic and osteogenic capacities of the co-doped scaffolds. Thus, signal molecules, including trace essential ions (Cu, Zn) and growth factor (GDF-5), incorporated in BCP offered combined

advantages to improve critical-sized defect healing. Although the action mechanisms of essential ions and GDF-5 need to be better elucidated, this combined release system provides an effective treatment for long bone defect healing.

Conflicts of interest

There are no conflicts to declare.

Acknowledgements

This study was supported by the China Scholarship Council (201908510077), National Natural Science Foundation of China (81071456), Science & Technology Department of Sichuan Province (2016JY0123, 2018JY0100, 2018SZYZF0012), Key Project of Education Department of Sichuan Province (17ZA0178), Southwest Medical University Affiliated Hospital Startup Program (19038), and Science & Technology Project of Nanchong City (18SXHZ0374, 18SXHZ0377, 18SXHZ0124).

References

1 P. Baldwin, D. J. Li, D. A. Auston, H. S. Mir, R. S. Yoon and K. J. Koval, *J. Orthop. Trauma*, 2019, **33**, 203–213.
2 R. J. Miron, A. Sculean, Y. Shuang, D. D. Bosshardt, R. Gruber, D. Buser, F. Chandad and Y. Zhang, *Clin. Oral Implan. Res.*, 2016, **27**, 668–675.
3 J. D. Currey, *J. Mater. Sci.*, 2012, **47**, 41–54.
4 R. Florencio-Silva, G. R. d. S. Sasso, E. Sasso-Cerri, M. J. Simões and P. S. Cerri, *BioMed Res. Int.*, 2015, **2015**, 1–17.
5 E. Gruskin, B. A. Doll, F. W. Futrell, J. P. Schmitz and J. O. Hollinger, *Adv. Drug Delivery Rev.*, 2012, **64**, 1063–1077.
6 R. Dimitriou, E. Jones, D. McGonagle and P. V. Giannoudis, *BMC Med.*, 2011, **9**, 66.
7 N. Fazzalari, *Osteoporosis Int.*, 2011, **22**, 2003–2006.
8 K. D. Hankenson, M. Dishowitz, C. Gray and M. Schenker, *Injury*, 2011, **42**, 556–561.
9 A. H. Reddi, *Cytokine Growth Factor Rev.*, 1997, **8**, 11–20.
10 D. W. Lee, Y. P. Yun, K. Park and S. E. Kim, *Bone*, 2012, **50**, 974–982.
11 M. K. Mafina, A. C. Sullivan and K. A. Hing, *Mater. Sci. Eng., C*, 2017, **80**, 207–212.
12 S. Boraiah, O. Paul, D. Hawkes, M. Wickham and D. G. Lorich, *Clin. Orthop. Relat. Res.*, 2009, **467**, 3257–3262.
13 C. A. Tannoury and H. S. An, *Spine J.*, 2014, **14**, 552–559.
14 N. E. Epstein, *Surg. Neurol. Int.*, 2013, **4**, S343–S352.
15 B. Mikic, *Ann. Biomed. Eng.*, 2004, **32**, 466–476.
16 P. Buxton, C. Edwards, C. W. Archer and P. Francis-West, *J. Bone Jt. Surg.*, 2001, **83**, S1–S23.
17 G. Feng, Y. Wan, G. Balian, C. T. Laurencin and X. Li, *Growth Factors*, 2008, **26**, 132–142.
18 C. M. Coleman and R. S. Tuan, *Mech. Dev.*, 2003, **120**, 823–836.
19 X. Cheng, T. Yang, W. Meng, H. Liu, T. Zhang and R. Shi, *Cells Tissues Organs*, 2012, **196**, 56–67.
20 D. Yang, S. J. Yoon and D. W. Lee, *Int. J. Mol. Sci.*, 2017, **18**, 1695.
21 Q. Zeng, X. Li, G. Beck, G. Balian and F. H. Shen, *Bone*, 2007, **40**, 374–381.
22 K. N. Leknes, J. Yang, M. Qahash, G. Polimeni, C. Susin and U. M. Wikesjö, *Clin. Oral Implan. Res.*, 2013, **24**, 1185–1191.
23 N. J. Lakhkar, I. H. Lee, H. W. Kim, V. Salih, I. B. Wall and J. C. Knowles, *Adv. Drug Delivery Rev.*, 2013, **65**, 405–420.
24 M. A. Saghiri, A. Asatourian, J. Orangi, C. M. Sorenson and N. Sheibani, *Crit. Rev. Oncol. Hemat.*, 2015, **96**, 143–155.
25 J. Gao, Z. Lv, C. Li, Y. Yue, X. Zhao, F. Wang and Y. Guo, *Biol. Trace Elem. Res.*, 2014, **162**, 309–316.
26 X. Luo, D. Barbieri, N. Davison, Y. Yan, J. D. de Bruijn and H. Yuan, *Acta Biomater.*, 2014, **10**, 477–485.
27 Y. Li, W. Xiong, C. Zhang, B. Gao, H. Guan, H. Cheng, J. Fu and F. Li, *J. Biomed. Mater. Res., Part A*, 2014, **102**, 3939–3950.
28 C. Gérard, L. J. Bordeleau, J. Barralet and C. J. Doillon, *Biomaterials*, 2010, **31**, 824–831.
29 S. Li, H. Xie, S. Li and Y. J. Kang, *Exp. Biol. Med.*, 2012, **237**, 77–82.
30 S. Bose, G. Fielding, S. Tarafder and A. Bandyopadhyay, *Trends Biotechnol.*, 2013, **31**, 594–605.
31 D. Xiao, F. Yang, Q. Zhao, S. Chen, F. Shi, X. Xiang, L. Deng, X. Sun, J. Weng and G. Feng, *RSC Adv.*, 2018, **8**, 29526–29534.
32 F. Shi, W. Zhi, Y. Liu, T. Zhou and J. Weng, *Mater. Lett.*, 2017, **203**, 13–16.
33 J. M. Lane and H. Sandhu, *Orthop. Clin. N. Am.*, 1987, **18**, 213–225.
34 N. C. Foot, *Stain Technol.*, 1933, **8**, 101–110.
35 H. Mayta, A. Talley, R. H. Gilman, J. Jimenez, M. Verastegui, M. Ruiz, H. Garcia and A. Gonzalez, *J. Clin. Microbiol.*, 2000, **38**, 133–137.
36 Y. Wu, J. Hou, M. Yin, J. Wang and C. Liu, *Mater. Sci. Eng., C*, 2014, **44**, 326–335.
37 G. M. Cooper, M. P. Mooney, A. K. Gosain, P. G. Campbell, J. E. Losee and J. Huard, *Plast. Reconstr. Surg.*, 2010, **125**, 1685–1692.
38 A. M. Costa, G. D. de Almeida Soares, R. Calixto and A. M. Rossi, *Key Eng. Mater.*, 2004, **254**, 119–122.
39 M. Othmani, H. Bachoua, Y. Ghandour, A. Aissa and M. Debbabi, *Mater. Res. Bull.*, 2018, **97**, 560–566.
40 E. A. Ofudje, A. I. Adeogun, M. A. Idowu and S. O. Kareem, *Heliyon*, 2019, **5**, e01716.
41 E. Barua, A. B. Deoghare, S. Chatterjee and P. Sapkal, *Ceram. Int.*, 2019, **45**, 20331–20345.
42 H. Cheng, L. Mao, X. Xu, Y. Zeng, D. Lan, H. Hu, X. Wu, H. You, X. Yang and R. Li, *Biomater. Sci.*, 2015, **3**, 665–680.
43 X. Zhang, J. Li, X. Wang, Y. Wang, R. Hang, X. Huang, B. Tang and P. K. Chu, *Mater. Sci. Eng., C*, 2018, **82**, 110–120.
44 J. Zhang, X. Ma, D. Lin, H. Shi, Y. Yuan, W. Tang, H. Zhou, H. Guo, J. Qian and C. Liu, *Biomaterials*, 2015, **53**, 251–264.

45 F. Yang, W. J. Dong, F. M. He, X. X. Wang, S. F. Zhao and G. L. Yang, *Oral Surg., Oral Med., Oral Pathol.*, 2012, **113**, 313–318.
46 P. H. Francis-West, A. Abdelfattah, P. Chen, C. Allen, J. Parish, R. Ladher, S. Allen, S. Macpherson, F. P. Luyten and C. W. Archer, *Development*, 1999, **126**, 1305–1315.
47 D. Wulsten, V. Glatt, A. Ellinghaus, K. Schmidt-Bleek, A. Petersen, H. Schell, J. Lienau, W. Sebald, F. Plöger and P. Seemann, *Eur. Cells Mater.*, 2011, **21**, 177–192.
48 K. Kerstin, W. E. Mechthild, B. Benjamin, H. Jeannine and R. Wiltrud, *J. Bone Jt. Surg., Am. Vol.*, 2014, **96**, 1699–1707.
49 Y. T. Kim, U. M. Wikesja, U. W. Jung, J. S. Lee, T. G. Kim and C. K. Kim, *J. Periodontol.*, 2013, **84**, 812–820.